



Highly dispersed photoactive zinc oxide nanoparticles on mesoporous phosphonated titania hybrid

Yun-Pei Zhu^a, Tian-Yi Ma^a, Tie-Zhen Ren^b, Jie Li^a, Gao-Hui Du^c, Zhong-Yong Yuan^{a,*}

^a Key Laboratory of Advanced Energy Materials Chemistry (Ministry of Education), Collaborative Innovation Center of Chemical Science and Engineering (Tianjin), College of Chemistry, Nankai University, Tianjin 300071, China

^b Hebei Provincial Key Lab of Green Chemical Technology & High Efficient Energy Saving, School of Chemical Engineering and Technology, Hebei University of Technology, Tianjin 300130, China

^c Key Laboratory of the Ministry of Education for Advanced Catalysis Materials, Institute of Physical Chemistry, Zhejiang Normal University, Jinhua 321004, China

ARTICLE INFO

Article history:

Received 10 December 2013

Received in revised form 26 February 2014

Accepted 2 March 2014

Available online 12 March 2014

Keywords:

Zinc oxide

Titania

Phosphonation

Coupled semiconductors

Photoactivity

ABSTRACT

Mesoporous phosphonated titania hybrid material was prepared with the use of aminotri(methylene phosphonic acid) as the coupling molecule and triblock copolymer F127 as the template, possessing irregular mesostructure formed by nanoparticle assembly of crystalline anatase phase. The phosphonate groups were homogeneously anchored on the mesoporous titania, allowing monolayer adsorption of Zn^{2+} by extensive coordination with the organic bridging groups. The highly dispersed photoactive ZnO components were then obtained by low-temperature annealing of the Zn^{2+} adsorbed mesoporous phosphonated TiO_2 , which exhibited excellent photocatalytic activity with high stability in photo-degradation of Rhodamine B under both UV and visible light irradiation. In comparison with the pristine mesoporous phosphonate titania, the commercial titania P25, and the ZnO /mesoporous titania prepared by the conventional impregnation, the superior photocatalytic performance and stability of the coupled catalyst of ZnO nanoparticles highly dispersed on the mesoporous phosphonated titania might be due to the coupling effect, the well-defined mesoporosity and the incorporation of phosphonic moieties into the TiO_2 network, presenting the potential applications in the fields of environmental remediation and solar cells.

© 2014 Elsevier B.V. All rights reserved.

1. Introduction

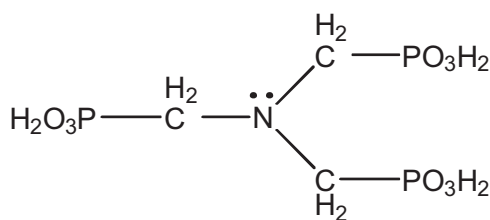
Increasing attention on various environmental contaminations, such as wastewater containing organic contaminants, has intrigued the creation and development of different treatment techniques and methodologies. Much effort has been taken on the photocatalytic process of organic pollutants in water and air with the help of semiconductor materials under appropriate light irradiation in the past two decades [1]. Titanium dioxide (TiO_2) is the most studied photocatalyst for environmental and energy applications because of its photocatalytic stability, easy availability and non-toxicity [2], and it is also an excellent semiconductor-type support material. Easy recombination of photo-induced electron-hole pairs, however, often leads to low quantum yields for most photocatalytic reactions [3]. Coupling with other semiconductor

materials so as to build a heterojunction structure at the interface is an alternative way to promote photoactivities through hindering the recombination of photo-induced carriers [4]. Sensitization of mesoporous metal oxide films with various quantum dots (CdSe [5], CdS [6], InP [7], InAs [8], and PbS [9]) have been proposed recently and their corresponding photoactivities were tested. Lu and co-workers reported dispersing and stabilizing CdS quantum dots on mesoporous TiO_2 substrate using mercaptopropionic acid as bifunctional linker, and this kind of photocatalyst showed high stability and activity [10]. Nonetheless, metal sulfides or selenides are toxic and harmful to human bodies, and it should be kept in mind that photoactivity is sensitive to the length of the bifunctional molecules, namely, the longer the linkers the lower the efficiency, due to the increase of the difficulty and distance of electron transferring/injection [11,12].

ZnO has similar band gap in comparison with TiO_2 , presenting excellent bulk electron mobility [13,14] and non-toxicity, which has been used for the coupling of ZnO and TiO_2 . Kim et al. prepared ZnO/TiO_2 hierarchical nanostructure by an electrospinning

* Corresponding author. Tel.: +86 22 23509610.

E-mail address: zyuan@nankai.edu.cn (Z.-Y. Yuan).



Scheme 1. Structure formula of ATMP.

process and a hydrothermal technique, which was further used as a photocatalyst for dye degradation [15]. Palmisano and co-workers synthesized the mixed ZnO/TiO_2 polycrystalline solids for photodegradation of 4-nitrophenol in liquid–solid regime [16]. However, the conventional synthesis of ZnO/TiO_2 composite photocatalysts usually involves multistep processes and the resultant photocatalytic activities decreased dramatically after multiple recycles.

Recent works have been aimed at the rational synthesis of organically functionalized porous metal oxide/organophosphonate hybrid materials because of their multifunctionalities from both the inorganic and organic components, and hence their potential in the fields of optics, electronics, catalysis, and adsorption [17–19]. The modification of the TiO_2 surface with phosphonic acids $RPO(OH)_2$ has been investigated extensively [20,21], and the anchoring is expected to involve both the coordination of the phosphoryl oxygen to Lewis acid sites and the condensation of P–OH groups with surface hydroxyl groups $Ti–OH$. Noticeably, the organophosphonate bridging groups can complex with a great many of metal ions, such as $Zn^{(II)}$, on the basis of complex-coordination interactions [22–25]. A step beyond could transform the coordinated metal ions into metal oxide, thus realizing their high dispersion on the hybrid surface. In this contribution, mesoporous phosphonated TiO_2 with high surface area and well-defined pore structures was fabricated by the hydrothermal technique in the presence of amphiphilic surfactant and organophosphonic acid, and then the high dispersion of ZnO nanoparticles were formed through low-temperature annealing of the Zn^{2+} adsorbed mesoporous phosphonated titania, rendering ZnO coupled mesoporous phosphonated titanium oxide photocatalysts. Photodegradation of Rhodamine B (RhB) under UV and visible light irradiation was experimented to investigate the photoactivity of the synthesized materials, and the possible photocatalytic mechanism was discussed. It was confirmed that the synthesized mesoporous phosphonated TiO_2 loaded with highly dispersed ZnO nanoparticles possessed higher photocatalytic activity and longer stability than the $ZnO/m-TiO_2$ prepared by traditional impregnation route, presenting a new strategy for preparing supported photocatalysts.

2. Experimental

2.1. Materials

Tetrabutyl titanate (TBT), ethanol and RhB were obtained from Tianjin Guangfu Chemical Co. Aminotri(methylene phosphonic acid) (ATMP, Scheme 1) was obtained from Henan Qingyuan Chemical Co. Nonionic triblock copolymer F127 ($EO_{106}PO_{70}EO_{106}$) was obtained from Nanjing Well Chemical Co., Ltd. Commercial photocatalyst P-25 (surface area: $50 \pm 15 \text{ m}^2 \text{ g}^{-1}$, crystalline size: 21 nm, λ_g : 392 nm, E_g : 3.16 eV, ~80% anatase and ~20% rutile) were purchased from Beijing J&K Scientific Ltd. Distilled water was used throughout. All the chemicals were of analytical grade and used as received without any further purification.

2.2. Synthesis

Mesoporous phosphonated titania was prepared on the basis of a modified sol–gel method [26]. In a typical run, 3.0 g of 36.5 wt% HCl was mixed with 30 ml of water and 10 ml of ethanol, and 1.0 g of F127 was added under vigorous stirring until complete dissolution. Then, 3.0 g of TBT was added drop by drop into the mixture, followed by the addition of 2.4 mmol of ATMP. After further stirring for 24 h under ambient conditions, the obtained mixture was transferred into a Teflon-lined autoclave and aged statically under autogenous pressure at 120 °C for 24 h. The product was filtered, washed and dried at 120 °C in an oven. Removal of the surfactant was accomplished by Soxhlet-extraction with ethanol for 60 h, and the resultant material was marked as Ti-ATMP.

The potential of Ti-ATMP for Zn^{2+} adsorption was tested as follows: 10 mg of the Ti-ATMP was added into 50 ml of $Zn(NO_3)_2$ solution with concentration from 1 to 40 mg L^{-1} . After stirring for 4 h to access the adsorption–desorption balance, the mixtures were filtered and the residual metal ion concentrations in the filtrates were analyzed by graphite furnace atomic absorption spectroscopy (AAS). The adsorption capacities of the adsorbent were then determined from the concentration difference measured between the filtrates and the initial metal ion solutions. The maximal adsorption capacity was calculated by the Langmuir model using the equation $n_s = Kn_m c / (1 + Kc)$, where K is the Langmuir constant, c is the Zn^{2+} concentration, n_m is the monolayer adsorption capacity, and n_s is the amount of Zn^{2+} adsorbed on the adsorbent. The monolayer adsorption capacity of Ti-ATMP was determined to be 28.1 mg g^{-1} and was used as the standard for ZnO dispersing amount.

ZnO was deposited on the synthesized Ti-ATMP support by the following procedure: 35 mmol of $Zn(NO_3)_2$ was added to 5 ml of water, followed by the addition of 1.0 g of Ti-ATMP. The slurry was stirred for 4 h under ambient conditions, and then 5 ml of NaOH solution (14 mmol L^{-1}) was added dropwise. After further stirring overnight, the solid product was isolated by centrifugation, washed with water and ethanol alternatively, dried at 120 °C and finally heated at 180 °C for 2 h, which was denoted as $ZnO/Ti-ATMP$. For comparison, mesoporous titania ($m-TiO_2$) supported ZnO composite photocatalyst with the same ZnO loading amount was prepared by treating 1.0 g of titania support with 5 ml of water containing 35 mmol of $Zn (NO_3)_2$ under stirring, followed by the addition of NaOH solution. After stirred overnight at room temperature and dried at 60 °C until all the solvent was evaporated, the mixture was heated at 180 °C for 2 h, which was marked as $ZnO/m-TiO_2$.

2.3. Characterization

Scanning electron microscopy (SEM) and Transmission electron microscopy (TEM) were carried out on a Jeol JSF-7500L at 5 keV and a Jeol JEM-2100F at 200 kV, respectively. N_2 adsorption–desorption isotherms were recorded on a Quantachrome NOVA 2000e sorption analyzer at liquid nitrogen temperature (77 K). The samples were degassed at 120 °C overnight prior to the measurement. The surface area was obtained by the multipoint Brunauer–Emmett–Teller (BET) method, and the pore size distribution was calculated from the isotherm by the nonlocal density functional theory (NLDFT) modeling method. X-ray diffraction (XRD) patterns were recorded on a Bruker D8 FOCUS diffractometer with $Cu K\alpha$ radiation (1.5418 Å) operated at 40 kV and 40 mA. Diffuse reflectance UV–vis absorption spectroscopy was employed on a JASCO V-570 UV–vis–NIR spectrophotometer, using $BaSO_4$ as a reference. XPS measurements were performed on a Kratos Axis Ultra DLD (delay line detector) spectrometer equipped with a monochromatic $Al K\alpha$ X-ray source (1486.6 eV). All XPS spectra were recorded using an aperture slot of $300 \mu\text{m} \times 700 \mu\text{m}$; survey spectra were recorded with a pass energy of 160 eV, and high-resolution spectra with a

pass energy of 40 eV. The chemical compositions were analyzed by inductively coupled plasma (ICP) emission spectroscopy on a Thermo Jarrell-Ash ICP-9000 (N+M) spectrometer. Fourier transform infrared (FT-IR) spectra were measured on a Bruker VECTOR 22 spectrometer with KBr pellet technique, and the ranges of spectrograms were 4000–400 cm^{-1} . Thermogravimetry (TG) and differential scanning calorimetry (DSC) were performed using a TA SDT Q600 instrument at a heating rate of 5 $^{\circ}\text{C}/\text{min}$ using $\alpha\text{-Al}_2\text{O}_3$ as the reference. Photoluminescence (PL) spectra were measured at ambient temperature on a Hitachi F-4500 FL fluorescence spectrophotometer. The excitation wavelength was 320 nm, and the PMT voltage was 700 V. Photoelectrochemical test was carried out on a Zennium (Zahner, German) workstation.

To investigate the transition of photogenerated electrons of the prepared photocatalysts, the corresponding electrodes were prepared as follows: 100 mg of the photocatalyst powder was mixed with trace amount of distilled water and ethanol, followed by blending in a mortar to get a homogeneous mixture. The slurry was then dip-coated onto a 1.5 cm \times 2 cm fluorine-doped tin oxide (FTO) glass electrode. Electrodes were dried in an oven at 180 $^{\circ}\text{C}$ for 2 h.

2.4. Photocatalytic activity test

The photocatalytic activity of the prepared catalysts was evaluated by the degradation of RhB dyes under either UV light or visible light irradiation under ambient conditions. A recycling water jacket was used to keep the reactor temperature constant. In the UV photocatalysis experiment, the synthesized catalyst (6 mg) was placed into a tubular quartz reactor of 100 ml of RhB solution (1×10^{-5} mol/L). A 125 W UV lamp with maximum emission at 365 nm was located 10 cm higher than solution surface. The reaction mixture was stirred under UV light irradiation. The suspensions were magnetically stirred in the dark for 30 min to ensure the establishment of adsorption/desorption equilibrium, and then exposed to the light irradiation at room temperature. At given time intervals, about 5 ml of liquor was sampled, centrifuged for 5 min to discard any sediment. The absorbance of reaction solutions was measured using a SP-722 spectrometer at $\lambda_{\text{max}} = 554$ nm. In the visible light irradiation experiment, 20 mg of the sample powder was placed into a tubular quartz reactor of 100 ml of RhB solution (1×10^{-5} mol/L), under a household desktop lamp with a 200-watt tungsten bulb (wavelength range: 400–2500 nm), used to roughly substitute the solar light (wavelength range: 300–2500 nm). Other conditions and operations were same with the UV photocatalysis experiment. The commercial Degussa P25 was also investigated under the identical conditions for comparison.

3. Results and discussion

The synthesis of mesoporous phosphonated titania material was performed in one-pot by the hydrolysis of tetrabutyl titanate in the F127 solution and the phosphonation using ATMP as organophosphonate coupling molecule. This synthesis process is relatively facile in comparison with the previously reported two-step sol-gel processing involving the formation of M–O–P bonds by non-hydrolytic condensation of a metal alkoxide with a phosphonic acid and then the formation of the M–O–M bonds of the metal oxide network by hydrolysis/condensation of the remaining alkoxide groups [27]. TG-DSC analysis of the obtained Ti-ATMP (Fig. 1) was performed to find the evidence for the presence of phosphonate in the materials and to investigate the thermal stability. The TG curve demonstrates initial weight loss of 8.6% from ambient temperature to 185 $^{\circ}\text{C}$, accompanied with an endothermal peak around 50 $^{\circ}\text{C}$ in the DSC curve, which may be assigned to the desorption of the surface adsorbed and intercalated water. The weight loss of 6.6% from

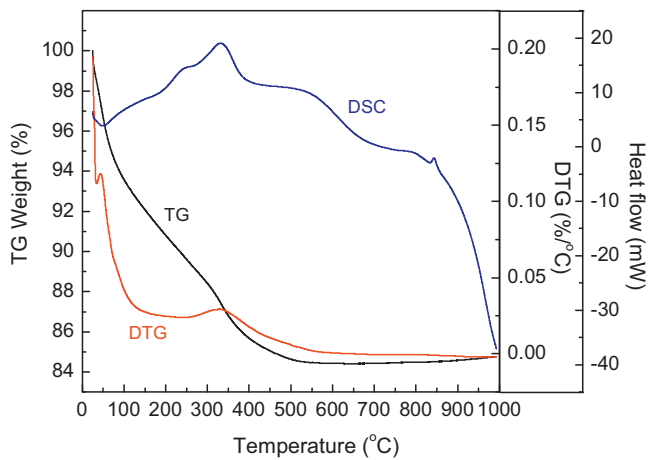
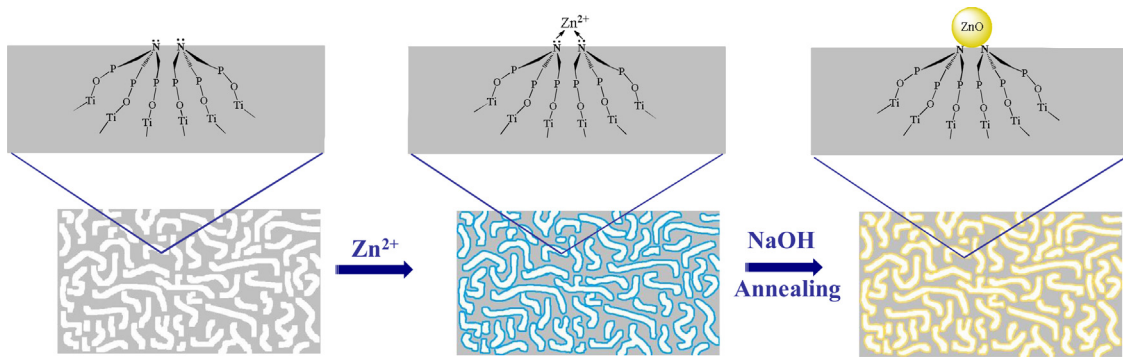


Fig. 1. TG-DSC profiles of the Ti-ATMP material.

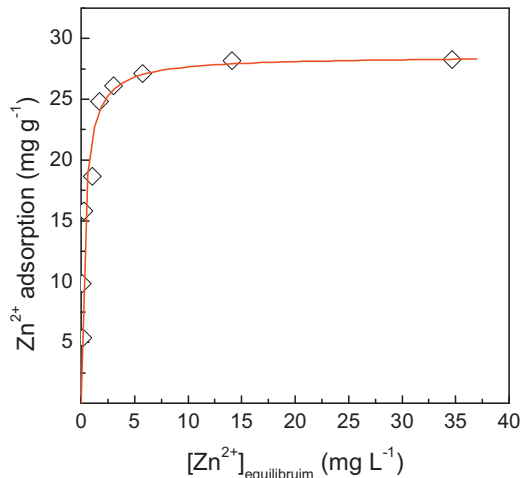
185 to 440 $^{\circ}\text{C}$ with two exothermal peaks at about 252 and 350 $^{\circ}\text{C}$ can be attributed to the decomposition of organic species. The weight loss of 0.7% from 440 to 1000 $^{\circ}\text{C}$ with two broad exothermal peaks at about 550 and 800 $^{\circ}\text{C}$ can correspond to the combustion of coke. It is also noticed that a weak exothermal peak situated at 843 $^{\circ}\text{C}$ in the DSC curve, corresponding to phase transition of titanium dioxide, and the temperature of this peak is much higher than our previous work [26]. Yu and coworkers synthesized phosphated mesoporous TiO_2 with high thermal stability because of complete condensation of surface Ti–OH with phosphoric acid and inhibition of grain growth by interspersed amorphous titanium phosphate matrix during heat treatment [28]. It is discernible that phosphonic species retaining on the surface of samples transformed to phosphoric ones during the high-temperature calcination process in air. Surface titanium phosphonate species transformed to phosphate ones during TG testing at high temperature in the atmosphere of pure air, which could stabilize the crystalline phase and elevate the temperature of phase transformation.

Previously reported porous titania/titanium phosphonate materials with controlled organophosphonic moieties exhibited large adsorption capacity for metal ions including Pb^{2+} , Cu^{2+} , and Cd^{2+} [20,22], which is mainly due to that the organic linkages could serve as active sites to chelate metal ions through acid–base reaction. The metal ions adsorbed could transform into metal oxide nanoparticles highly dispersed on the surface of these hybrid materials for potential applications [29]. Thus, in this work the highly dispersed ZnO nanoparticles on the porous Ti-ATMP hybrid were achieved through simple adsorption and annealing process, as depicted in Scheme 2. The Zn^{2+} ions were first adsorbed on the preformed Ti-ATMP matrix, following a monolayer adsorption behavior, and then the low-temperature annealing would result in the high dispersion of ZnO nanoparticles. The annealing temperature was selected at 180 $^{\circ}\text{C}$, considering that the preformed highly dispersed $\text{Zn}(\text{OH})_2$ could dehydrate completely at 180 $^{\circ}\text{C}$ to form ZnO nanoparticles in situ, and such a temperature was not high enough to destroy the organic phosphonate species, which could tightly bind the ZnO nanoparticles and improve the stability of the coupled photocatalyst.

Fig. 2 shows the Zn^{2+} adsorption isotherm for the Ti-ATMP material. The isotherm was found to follow Langmuir-type adsorption model with the ions being almost quantitatively adsorbed until binding saturation was reached. The maximal adsorption capability was determined to be 28.1 mg g^{-1} . Similar to previously reported ethylene-diamine contained PMO type adsorbents [30], the adsorption behavior of Ti-ATMP for Zn^{2+} was mainly determined by the N species situated on the hybrid surface and the specific surface area



Scheme 2. Simulated formation mechanism of ZnO/Ti-ATMP materials.

Fig. 2. Zn²⁺ adsorption isotherm of Ti-ATMP.

of the host materials. After further annealing of Zn²⁺ loaded Ti-ATMP, highly dispersed ZnO active components were thus formed.

The FT-IR spectra of Ti-ATMP and the coupled ZnO/Ti-ATMP catalyst are shown in Fig. 3. The strong and broad band at 3404 cm⁻¹ and the sharp vibration band at 1638 cm⁻¹ correspond to the surface-adsorbed water molecules and hydroxyl groups. The band at 1058 cm⁻¹ is due to P—O—Ti stretching vibrations [23], while a shoulder at 1148 cm⁻¹ is attributed to P—CH₂N= groups [31]. The small weak band at 1322 cm⁻¹ can be attributed to the C—N stretching vibrations [32], and the band at 1437 cm⁻¹ is due to the P—C stretching vibrations. The band assigned to P—OH at 930 cm⁻¹ are not observed in either Ti-ATMP or ZnO/Ti-ATMP [33], revealing

the extensive condensation between Ti—OH and P—OH groups to form P—O—Ti bridges. It is also indicated that F127 was removed completely by ethanol extraction for the reason that the C—O vibration band around 1030 cm⁻¹ existing in the surfactant could not be observed [16]. No prominent Zn—O bands were seen, which may be owing to the supported content of ZnO out of the detection limit of conventional IR analysis method.

XPS analysis was taken on the surface of ZnO/Ti-ATMP (Fig. 4). The XPS Ti 2p line of the ZnO/Ti-ATMP is composed of two single peaks situated at 458.6 eV for Ti 2p_{3/2} and 464.1 eV for Ti 2p_{1/2}, indicating that the Ti element mainly exists as the chemical state of Ti⁴⁺ [34,35]. Compared with the binding energy of pure titania (459 eV for Ti 2p_{3/2} and 464.8 eV for Ti 2p_{1/2}), the Ti 2p peaks of ZnO/Ti-ATMP shifts to lower binding energy, which might be the result of organophosphonate incorporation in titania framework [36]. The Zn 2p spectrum shows two weak symmetric peaks centering at 1021.9 and 1044.8 eV, which are attributed to the Zn 2p_{3/2} and 2p_{1/2} signals respectively, indicating that Zn(II) was bonded to oxygen atom to form ZnO [37]. These results confirmed that zinc cations did not enter TiO₂ lattice, but existed as highly dispersed ZnO nanoparticles, because there was no other Zn 2p peak appeared in XPS spectrum [2]. One symmetrical peak of the P 2p spectrum was observed with a binding energy of 133.1 eV, which is attributed to the single chemical environment of phosphorus in the —P(O—Ti)₃— units. No peaks relating to Ti—P bonds appear at 128.6 eV. The broad and asymmetric peak of O 1s can be fitted to two peaks. The main peak at around 530.1 eV can be assigned to the oxygen in the P—O—Ti linkages, while the other one at 531.8 eV corresponds to surface hydroxyl and adsorbed water molecules [23]. The N 1s spectrum show a weak peak at 400.8 eV that corresponds to bridged N species in the organophosphonic acid. The surface atomic composition according to XPS was calculated to be 13.14% Ti, 1.99% P, 0.69% N, 0.38% Zn, 43.32% C, and 41.48% O. The ZnO dispersing amount on the Ti-ATMP was also analyzed by inductively coupled plasma emission spectroscopy to be 2.78 wt%.

Fig. 5 shows the XRD patterns of the prepared Ti-ATMP and ZnO/Ti-ATMP samples. The diffraction peaks locating at 25.4°, 36.9°, 38.3°, 38.6°, 48.1°, 53.9°, 55.6°, 62.8° and 75.2° are attributed to TiO₂ anatase phase (JCPDF No. 21-1272). After ZnO loading on Ti-ATMP by low-temperature annealing, no evident diffraction peaks of crystallite ZnO could be observed, which may be due to the high dispersion of the ZnO nanoparticles with too small particle sizes on the surface of the phosphonated titania support [38]. The average crystallite sizes of both Ti-ATMP and ZnO/Ti-ATMP samples are about 8 nm, estimated from the (101) peak width of anatase by Scherrer equation.

A deeper insight to the fine structure of Ti-ATMP was characterized by TEM. Fig. 6a shows clearly wormhole-like interconnected mesopores resulted from nanoparticle assembly. From the high-resolution TEM image (Fig. 6b), the lattice fringes can be clearly

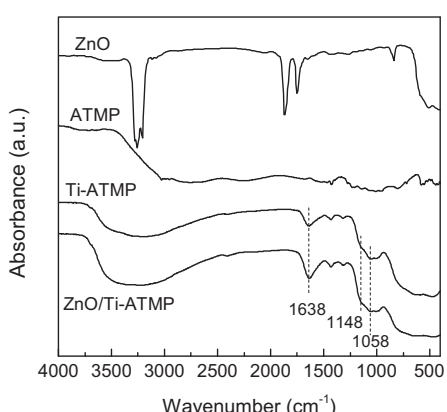


Fig. 3. FT-IR spectra of Ti-ATMP, ZnO/Ti-ATMP, ATMP and ZnO.

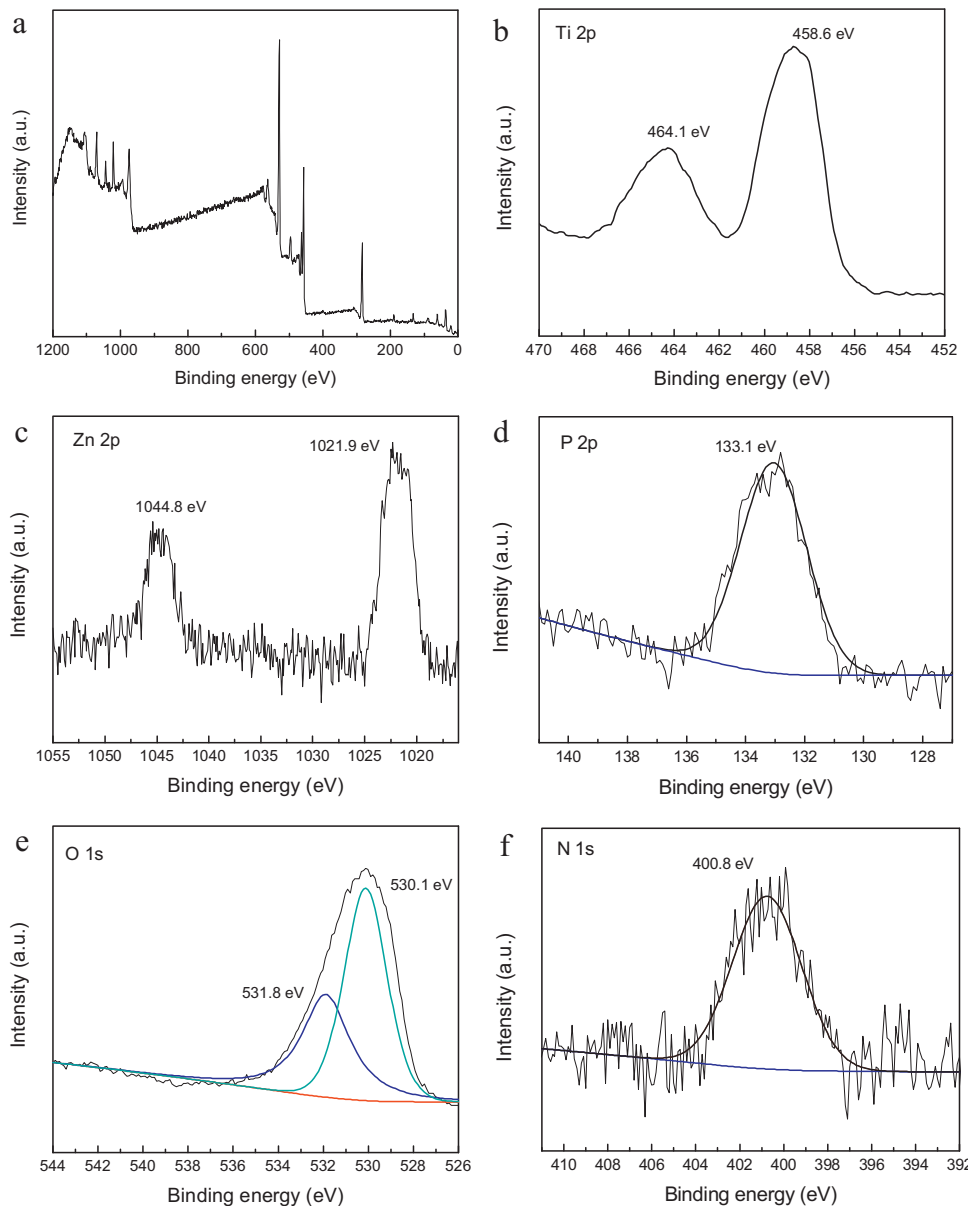


Fig. 4. XPS survey scans (a) and high-resolution spectra of the Ti 2p (b), Zn 2p (c), P 2p (d), O 1s (e) and N 1s (f) of the ZnO/Ti-ATMP coupled material.

seen, indicating the crystalline phase of Ti-ATMP. The uniform nanoparticles are nearly 8 nm in size, which is consistent to the XRD analysis. The interplanar spacing of about 3.5 Å is observed in the inset image of Fig. 6b, which is attributed to lattice spacing of the (101) crystallite planes of anatase-TiO₂. However, it was still difficult to directly observe the ZnO nanoparticles for the ZnO/Ti-ATMP in TEM images owing to the low ZnO content and the corresponding high dispersion.

N₂ adsorption-desorption analysis was carried out to further characterize the porous properties of the synthesized Ti-ATMP and ZnO/Ti-ATMP materials (Fig. 7). Both samples show similarly the typical type IV isotherms, indicative of the presence of well-defined mesoporosity according to the IUPAC classification [39]. The hysteresis loops of type H2 were observed, suggesting the ink-bottle-like mesopores. The pore size distributions of Ti-ATMP and ZnO/Ti-ATMP, calculated by the NLDFT method, are narrow ranging from 2 to 13 nm with a maximum around 6.1 nm. One can clearly see that both samples possess the nearly identical isotherms and pore size distributions except that the volume of nitrogen adsorbed

of Ti-ATMP is higher than that of ZnO/Ti-ATMP. This suggests that the highly dispersed ZnO nanoparticles of small amount could not intensively affect the textural and structural properties of the resultant material. The multipoint BET surface areas of Ti-ATMP and ZnO/Ti-ATMP are 307 and 265 m² g⁻¹, and the pore volumes are 0.38 and 0.33 cm³ g⁻¹, respectively.

The UV-vis absorption spectroscopy was performed to measure the photo-response of the fabricated materials and the spectral properties (Fig. 8). The strong adsorption at 300–350 nm can be observed for the two kinds of semiconductor materials. However, for the ZnO/Ti-ATMP semiconductor, the absorption on-set (389 nm) red-shifts as compared with Ti-ATMP (382 nm), and it shows higher absorption in the range of visible light. This may be owing to the high dispersion of ZnO on the pore walls of phosphonated TiO₂ and significant differences in the surface state (e.g., surface deficiency), which promoted the separate efficiency of photogenerated charges and extend the range of excited spectrum [1,40]. The band-gap values for Ti-ATMP and ZnO/Ti-ATMP are 3.25 and 3.18 eV, respectively, calculated by the formula E_g

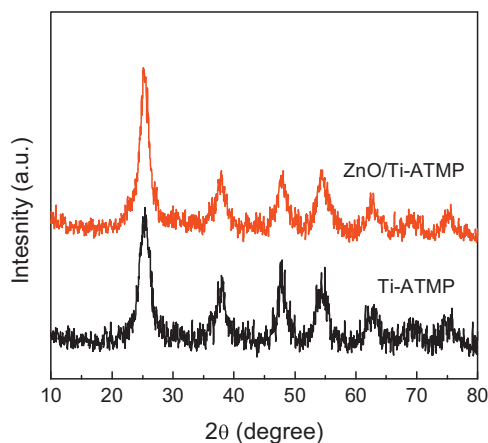


Fig. 5. XRD patterns of Ti-ATMP and ZnO/Ti-ATMP.

(eV) = $1240/\lambda_g$ (nm), where λ_g stands for the wavelength value corresponding to the intersection point of the vertical and horizontal parts of the spectra. The observed lower band-gap of the ZnO/Ti-ATMP coupled catalyst and stronger adsorption within the scope of visible light suggest the significant performance in photocatalytic degradation of organic pollutants under suitable light irradiation.

Thus, the degradation of RhB under UV and visible light irradiation was carried out by the ZnO/Ti-ATMP composite as a potential

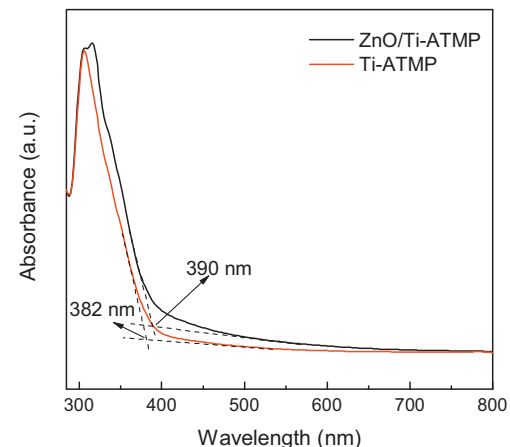


Fig. 8. The UV-vis absorption spectra of Ti-ATMP and ZnO/Ti-ATMP.

photocatalyst (Fig. 9), and compared with that of pristine Ti-ATMP and the commercial titania P25 catalyst. A blank experiment (self-degradation process), for the purpose of comparison, was also performed in the absence of any catalysts. As shown in Fig. 9a, under UV light irradiation, only a little amount of RhB (8.2%) was degraded without adding any catalysts. However, in the presence of photocatalysts, a big degree of photodegradation of RhB occurred under UV irradiation, suggesting that the degradation of RhB is caused by

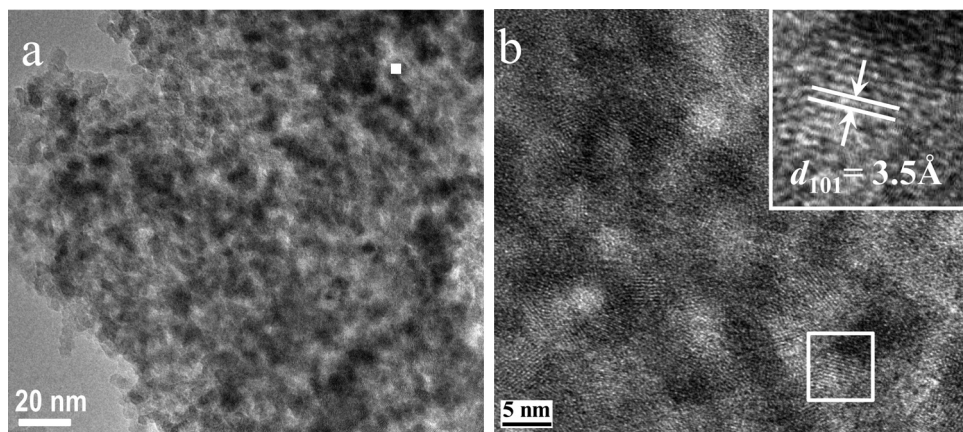


Fig. 6. TEM image (a) and corresponding HR-TEM image (b) of Ti-ATMP material. Inset of (b) shows interplanar spacing $d_{101} = 3.5\text{ \AA}$.

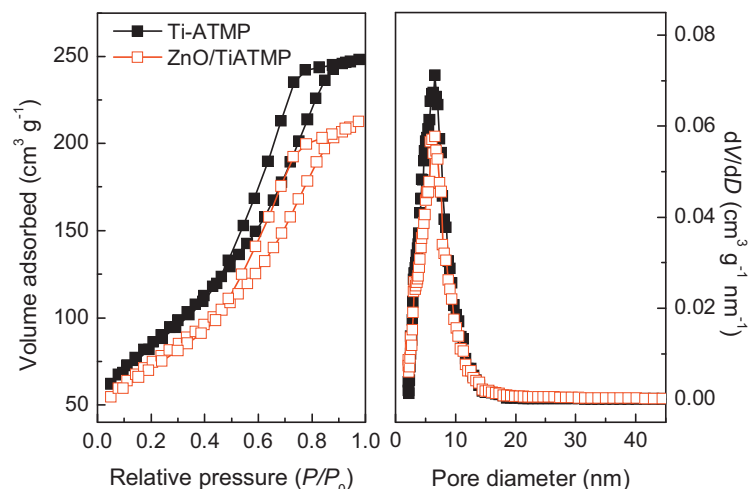


Fig. 7. N_2 adsorption-desorption isotherms (left) and corresponding pore-size distribution curves (right) determined by NLDFT method.

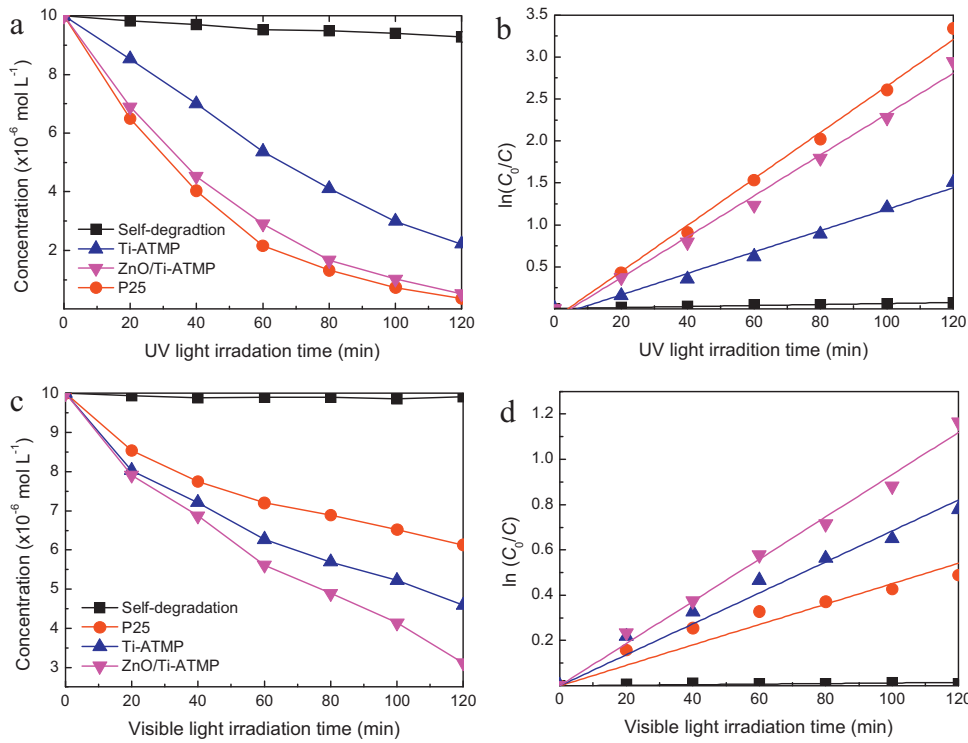


Fig. 9. Photoactivities for RhB degradation under UV (a) and visible (c) light irradiation; plots of $\ln(C_0/C)$ versus the irradiation time for UV (b) and visible (d) light irradiation, showing the fitting results using the pseudo-first-order reaction.

the semiconductor sensitization process under the UV light irradiation. After 120 min of UV irradiation, the photo-degradation efficiencies of RhB for P25, Ti-ATMP and ZnO/Ti-ATMP are 96.4%, 77.8% and 94.8%, respectively, indicating comparable activity of ZnO/Ti-ATMP to that of commercial P25. However, the photoactivities under visible light irradiation are a little different (Fig. 9c). P25 can only degrade 39.7% RhB. While, the photo-degradation efficiencies for Ti-ATMP and ZnO/Ti-ATMP are 54.1% and 68.8%, respectively, higher than that of P25.

The photocatalytic degradation reaction can be assumed to follow pseudo-first-order expression [41]: $\ln(C_0/C) = kt$, where C_0/C is the normalized organic compounds concentration and k is the apparent reaction rate (min^{-1}). Fig. 9b and d show the relationship between $\ln(C_0/C)$ and the irradiation time (t) for the UV and visible light degradation of RhB, respectively. The photoactivity has been defined as the overall degradation rate constant of the catalysts. By plotting $\ln(C_0/C)$ versus irradiation time through linear regression, the slope of the simulated straight lines is considered to be the k constant. By plotting $\ln(C_0/C)$ as a function of irradiation time through linear regression, the k constant can be obtained from the slopes of the simulated straight lines. The UV degradation k constants for P25, ZnO/Ti-ATMP, Ti-ATMP are 0.02764, 0.02436 and 0.01275 min^{-1} , respectively, following the sequence of P25 > ZnO/Ti-ATMP > Ti-ATMP. While under visible light irradiation, the corresponding reaction rates follow the sequence of ZnO/Ti-ATMP ($0.009933 \text{ min}^{-1}$) > Ti-ATMP (0.00684 min^{-1}) > P25 (0.00452 min^{-1}). This indicates that the coupling effect of ZnO/Ti-ATMP made a difference during the photocatalytic reaction process.

Semiconductor materials can absorb the photons with appropriate energy to generate electron–hole pairs, and the subsequent recombination of the photo-excited electrons and holes can release energy in the form of photoluminescence. Photoluminescence emission spectrum stems from the recombination of free charge carriers and can serve as a good candidate for the illustration of the coupled semiconductor systems, indicating the process of

charge migration and separation. Thus, photoluminescence spectroscopy has been widely used to confirm lower recombination of photo-generated electron–hole pairs for coupled photocatalysts or heterojunction structures [36,39,42]. Namely, the lower photoluminescence intensity is, the higher photoactivities and quantum yield are. The PL spectra of Ti-ATMP and ZnO/Ti-ATMP are given in Fig. 10. The PL emission intensities of Ti-ATMP and ZnO/Ti-ATMP exhibit a maximum at about 524 nm. But Ti-ATMP demonstrates stronger emission intensity than the coupled photocatalyst. With respect to ZnO/Ti-ATMP composite, the photo-induced carriers can migrate easily between ZnO and TiO₂, which leads to the inhibition of the recombination of electron–hole pairs, resulting in the higher photocatalytic efficiency. This cannot only demonstrate the easier recombination of electron–hole pairs of Ti-ATMP than that of ZnO/Ti-ATMP, but also confirm the high dispersion of ZnO on the surface of the porous phosphonated titania.

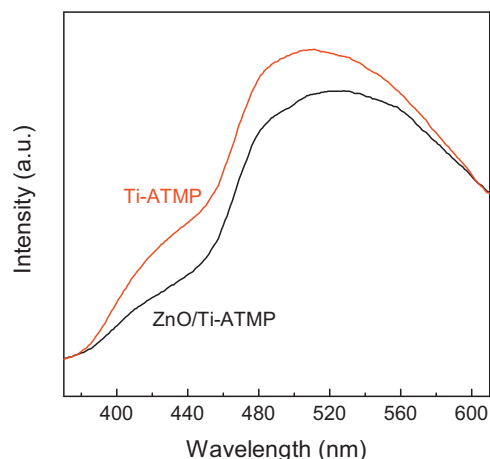


Fig. 10. PL spectrum of Ti-ATMP and ZnO/Ti-ATMP.

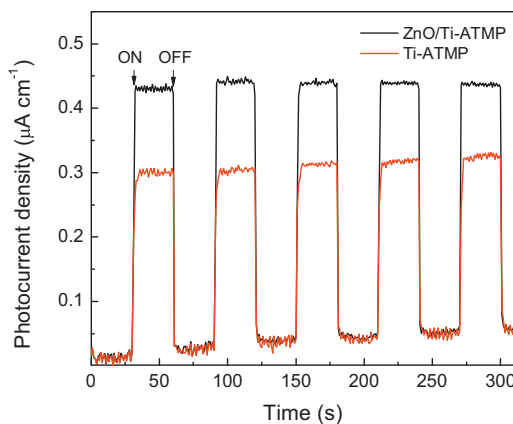
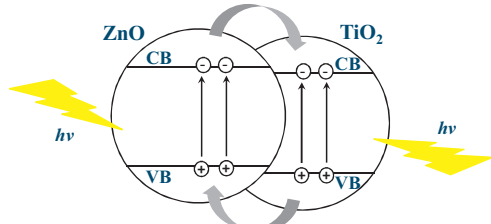


Fig. 11. Photocurrent response curves of ZnO/Ti-ATMP and Ti-ATMP under visible light illumination.

On the other hand, the photocatalytic redox reactions are intimately related to the separation efficiency of photoinduced electron–holes pairs arose from the excited semiconductors. To qualitatively investigate the separation efficiency of photoinduced charges during the photoreactions, the photocurrent response was carried out for Ti-ATMP and ZnO/Ti-ATMP (Fig. 11). It can be obviously seen that fast and stable responses were observed in two electrodes and the response signals are entirely reversible. Under visible light illumination, the photocurrent of the ZnO/Ti-ATMP electrode is about 1.4 times higher than that of pristine Ti-ATMP electrode. The remarkable enhancement of the photocurrent of the coupled photocatalysts reveals an enhanced separation efficiency of the photogenerated electrons and holes [43,44], which can contribute to the improvement of photocatalytic capacity.

Both ZnO/Ti-ATMP and Ti-ATMP have well-structured mesoporosity with high specific surface area (no less than $260\text{ m}^2\text{ g}^{-1}$) and more catalytic active sites, which could increase the photoabsorption and mass transfer [36,45,46]. Meanwhile, organophosphonate groups were homogeneously anchored in titania particles, which made contributions to the improvement of photocatalytic activity and the stability of the framework of mesoporous phosphonated titania. Moreover, the photoactivity enhancement of ZnO/Ti-ATMP, as compared with Ti-ATMP and P25, could be attributed mainly to the coupling effect between the highly dispersed ZnO nanoparticles and porous phosphonated titania hybrid [37]. The mechanistic scheme for charge separation and photocatalytic behavior are depicted in Scheme 3. The photo-generated electrons from the valence band of ZnO entered the valence band of Ti-ATMP, and conversely, the photo-generated holes transferred from the conduction band of TiO₂ into that of ZnO. Such an efficient charge separation increases the lifetime of photo-generated carriers and the efficiency of interfacial charge transfer to the substrate. Hence, the photoactivities increase because of the impediment of the recombination between photo-generated electron–hole pairs by facilitating their separation [15,37]. The photocatalytic



Scheme 3. Schematic diagram illustrating the principle of electron–hole charge separation and photoactivity for ZnO/Ti-ATMP.

Table 1
Summary of the physicochemical properties of the synthesized materials.

| Sample | $S_{\text{BET}}^{\text{a}}$ ($\text{m}^2\text{ g}^{-1}$) | $V_{\text{pore}}^{\text{b}}$ ($\text{cm}^3\text{ g}^{-1}$) | $D_{\text{DFT}}^{\text{c}}$ (nm) | ZnO amount ^d (wt%) |
|---------------------------------|---|---|----------------------------------|----------------------------------|
| Ti-ATMP | 307 | 0.38 | 6.1 | – |
| ZnO/Ti-ATMP | 265 | 0.33 | 6.1 | 2.78 |
| <i>m</i> -TiO ₂ | 314 | 0.45 | 6.2 | – |
| ZnO/ <i>m</i> -TiO ₂ | 262 | 0.39 | 6.1 | 2.78 |

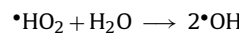
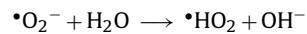
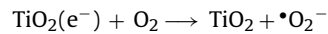
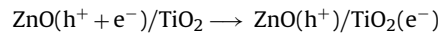
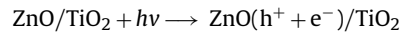
^a BET surface area calculated from the linear part of the BET plot.

^b Single point total pore volume of pores at $P/P_0 = 0.98$.

^c Pore diameter calculated by the NLDFT model.

^d Amount of the dispersed ZnO determined by ICP analysis.

degradation of organic compounds into achromatous organic species by the coupled photocatalyst could be described as the following reactions:



ZnO/*m*-TiO₂ composite catalyst was also prepared by the conventional deposition method, and its textural property is listed in Table 1. The photocatalytic activity of ZnO/*m*-TiO₂ was investigated at the same condition of photocatalytic RhB degradation for ZnO/ATMP. It is seen that ZnO/*m*-TiO₂ degraded 64.7% RhB after 120 min visible light irradiation (Fig. 12), which is higher than that of Ti-ATMP (54.1%) but lower than ZnO/Ti-ATMP (68.8%). Furthermore, the used ZnO/*m*-TiO₂ and ZnO/Ti-ATMP catalysts were collected and washed with water and ethanol alternatively, and then re-used as catalysts for next run experiment. As shown in Fig. 12, after four times recycles, the photocatalytic efficiency of ZnO/*m*-TiO₂ decreased dramatically from 64.7% to 38.4%, which may be due to the abscission of the loosely dispersed ZnO components from the mesoporous titania substrate.

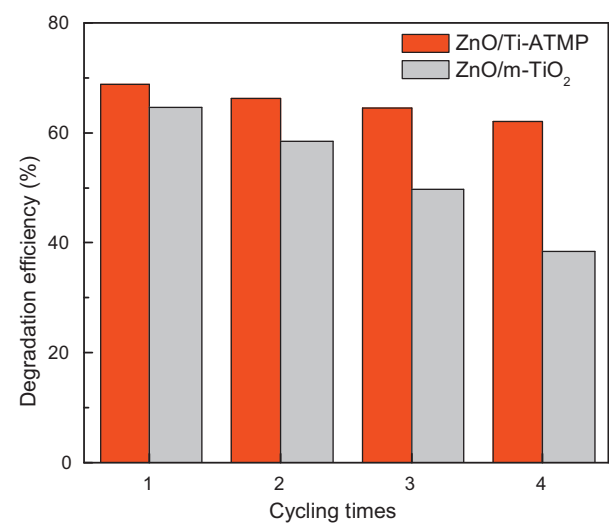


Fig. 12. The overall degradation efficiency of ZnO/Ti-ATMP and ZnO/*m*-TiO₂ under visible light irradiation versus the cycling times.

However, ZnO/Ti-ATMP could degrade 62.1% RhB even after experiencing multiple reuses. The corresponding little deterioration of photoactivity may be assigned to the photocorrosion of exposed ZnO during the photocatalytic process [43]. In this work, the difference between ZnO/m-TiO₂ and ZnO/Ti-ATMP obtained by two preparation methods is the modification of the mesoporous titania matrix by organophosphonation. Since all the catalysts are typical mesoporous materials according to the N₂ sorption analysis (Table 1), with similar surface areas around 260 m² g⁻¹ and pore sizes around 5.5 nm. Thus the pore structure related distinction could be neglected, and the above difference of the photoactivity and stability could be attributed to the anchoring of phosphonate linkages onto the mesoporous TiO₂. It is considered that the dispersion of Zn²⁺ ions onto the inorganic support like titania was difficult to control, so the monolayer adsorption was hardly accessed. The Zn²⁺ ions were mainly physically adsorbed on the inorganic framework, and the further annealing could cause the agglomeration of ZnO nanoparticles and the weak interaction between the host-guest semiconductors, resulting in the limited enhancement of the activity and stability of the obtained ZnO/m-TiO₂ catalysts. On the contrary, the adsorption of Zn²⁺ ions onto the phosphonated titania material is facile to control the dispersion condition as well as the adsorption amount of the metal ions. The highly dispersed ZnO active components could be effectively and stably inhabited on the mesoporous titania. Therefore, the resultant ZnO/Ti-ATMP coupled photocatalyst presented better catalytic ability and relatively high stability.

4. Conclusions

Mesoporous phosphonated titania hybrid has been synthesized in the presence of triblock copolymer with the corresponding triphosphonic acid as the coupling molecule. The accessible mesovoids and homogeneously anchored phosphonic claw groups endowed the hybrid with the capability for the Zn²⁺ monolayer adsorption, and after a low-temperature annealing, the adsorbed Zn²⁺ ions transformed into ZnO active components that were highly dispersed on the mesoporous phosphonated TiO₂ support, exhibiting significant enhanced photocatalytic activity with high stability in the photodegradation of RhB under both UV and visible light irradiation. The considerable photocatalytic activity and stability of the highly dispersed ZnO coupled mesoporous phosphonated titania catalyst prepared by this coordination and annealing methodology, in comparison with those of the pristine mesoporous phosphonated titania, the commercial titania P25, and the ZnO/m-TiO₂ prepared by conventional impregnation, might result from the coupled semiconductor systems, well-defined porosity and phosphonate incorporation, suggesting the superiority of the present preparation strategy. This work provides a new way for the fabrication of supported semiconductors with high photocatalytic performance, and demonstrates their potential in the areas of environmental remediation and photoelectrochemistry.

Acknowledgements

This work was supported by the National Natural Science Foundation of China (21076056 and 21073099), the Specialized

Research Fund for the Doctoral Program of Higher Education (20110031110016), and the 111 project (B12015).

References

- [1] R.T. Sapkal, S.S. Shinde, T.R. Waghmode, S.P. Govindwar, K.Y. Rajpure, C.H. Bhosale, *J. Photochem. Photobiol. B* 110 (2012) 15–21.
- [2] Y. Ku, Y.H. Huang, Y.C. Chou, *J. Mol. Catal. A* 342 (2011) 18–22.
- [3] C.M. Ma, Y. Ku, Y.C. Chou, F.T. Jeng, *J. Environ. Manage.* 18 (2008) 363–369.
- [4] F. Fresno, M.D. Hernández-Alonso, T. David, J.M. Coronado, J. Soria, *Appl. Catal. B* 84 (2008) 598–606.
- [5] K. Kim, M.J. Kim, S.I. Kim, J.H. Jang, *Sci. Rep.* 3 (2013) 3330.
- [6] R. Sasaki, A.P. Gaikwad, V. Sudarsan, N. Gupta, S.R. Bharadwaj, *Appl. Catal. A* 464 (2013) 149–155.
- [7] H.M. Chen, C.K. Chen, C.C. Lin, R.S. Liu, H. Yang, W.S. Chang, K.H. Chen, T.S. Chan, J.F. Lee, D.P. Tsai, *J. Phys. Chem. C* 115 (2011) 21971–21980.
- [8] Z.S. Yang, C.Y. Chen, P. Roya, H.T. Chang, *Chem. Commun.* 47 (2011) 9561–9571.
- [9] S.D. Sung, I. Lim, P. Kang, C.M. Lee, W.I. Lee, *Chem. Commun.* 49 (2013) 6054–6056.
- [10] S.S. Qian, C.S. Wang, W.J. Liu, Y.H. Zhu, W.J. Yao, X.H. Lu, *J. Mater. Chem.* 21 (2011) 4945–4952.
- [11] R.S. Dibbell, D.F. Watson, *J. Phys. Chem. C* 113 (2009) 3139–3149.
- [12] R.S. Dibbell, D.G. Youker, D.F. Watson, *J. Phys. Chem. C* 113 (2009) 18643–18651.
- [13] D.C. Look, D.C. Reynolds, J.R. Sizelove, R.L. Jones, C.W. Litton, G. Cantwell, W.C. Harsch, *Solid State Commun.* 105 (1998) 399–401.
- [14] L. Forro, O. Chauvet, D. Emin, L. Zuppiroli, H. Berger, F. Levy, *J. Appl. Phys.* 75 (1994) 633–635.
- [15] M.A. Kanjwal, N.A.M. Barakat, F.A. Sheikh, S.J. Park, H.Y. Kim, *Macromol. Res.* 18 (2010) 233–240.
- [16] G. Marci, V. Augugliaro, M.J. López-Muñoz, C. Martín, L. Palmisano, V. Rives, M. Schiavello, R. Tilley, A.M. Venezia, *J. Phys. Chem. B* 105 (2001) 1033–1040.
- [17] G. Guerrero, J.G. Alauzun, M. Granier, D. Laurencina, P.H. Mutin, *Dalton Trans.* 42 (2013) 12569–12585.
- [18] C. Queffelec, M. Petit, P. Janvier, D.A. Knight, B. Bujoli, *Chem. Rev.* 112 (2012) 3777–3807.
- [19] H. Ma, O. Acton, D.O. Hutchins, N. Cernetic, A.K.Y. Jen, *Phys. Chem. Chem. Phys.* 14 (2012) 14110–14126.
- [20] X.J. Zhang, T.Y. Ma, Z.Y. Yuan, *Eur. J. Inorg. Chem.* (2008) 2721–2726.
- [21] K. Maeda, *Microporous Mesoporous Mater.* 73 (2004) 47–55.
- [22] T.Y. Ma, X.J. Zhang, Z.Y. Yuan, *J. Phys. Chem. C* 113 (2009) 12854–12862.
- [23] T.Y. Ma, H. Li, A.N. Tang, Z.Y. Yuan, *Small* 7 (2011) 1827–1837.
- [24] K.P. Guerra, R. Delgado, *Dalton Trans.* (2008) 539–550.
- [25] T. Storr, M. Merkel, G.X.S. Zhao, L.E. Scott, D.E. Green, M.L. Bowen, K.H. Thompson, B.O. Patrick, H.J. Schugar, C. Orvig, *J. Am. Chem. Soc.* 129 (2007) 7453–7463.
- [26] X.J. Zhang, T.Y. Ma, Z.Y. Yuan, *J. Mater. Chem.* 18 (2008) 2003–2010.
- [27] G. Guerrero, P.H. Mutin, A. Vioux, *Chem. Mater.* 12 (2000) 1268–1272.
- [28] J.C. Yu, L.Z. Zhang, Z. Zheng, J.C. Zhao, *Chem. Mater.* 15 (2003) 2280–2286.
- [29] T.Y. Ma, Z.Y. Yuan, *Dalton Trans.* 39 (2010) 9570–9578.
- [30] K.Z. Hossain, L. Mercier, *Adv. Mater.* 14 (2002) 1053–1056.
- [31] G. Guerrero, P.H. Mutin, A. Vioux, *Chem. Mater.* 13 (2001) 4367–4373.
- [32] T.Y. Ma, X.J. Zhang, Z.Y. Yuan, *J. Phys. Chem. C* 113 (2009) 12584–12862.
- [33] T.Y. Ma, Z.Y. Yuan, *Chem. Commun.* 46 (2010) 2325–2327.
- [34] T.Y. Ma, Z.Y. Yuan, *ChemSusChem* 4 (2011) 1407–1419.
- [35] J.C. Yu, L.Z. Zhang, Z. Zheng, J.C. Zhao, *Chem. Mater.* 15 (2003) 2280–2286.
- [36] T. Kawahara, Y. Konishi, H. Tada, N. Tohge, J. Nishii, S. Ito, *Angew. Chem. Int. Ed.* 41 (2002) 2811–2813.
- [37] X. Gao, W. Sun, Z. Hu, G. Ai, Y. Zhang, S. Feng, F. Li, L. Peng, *J. Phys. Chem. C* 113 (2009) 20481–20485.
- [38] C. Shifu, Z. Wei, L. Wei, Z. Sujuan, *Appl. Surf. Sci.* 255 (2008) 2478–2484.
- [39] M. Kruk, M. Jaroniec, *Chem. Mater.* 13 (2001) 3169–3183.
- [40] X.D. Yan, C.W. Zou, X.D. Gao, W. Gao, *J. Mater. Chem.* 22 (2012) 5629–5640.
- [41] G.S. Shao, X.J. Zhang, Z.Y. Yuan, *Appl. Catal. B* 82 (2008) 208–218.
- [42] J.S. Zhang, M.W. Zhang, R.Q. Sun, X.C. Wang, *Angew. Chem. Int. Ed.* 51 (2012) 1–6.
- [43] Y.J. Wang, R. Shi, J. Lin, Y.F. Zhu, *Energy Environ. Sci.* 4 (2011) 2922–2929.
- [44] L. Liu, Z. Ji, W. Zou, X. Gu, Y. Deng, F. Gao, C. Tang, L. Dong, *ACS Catal.* 3 (2013) 2052–2061.
- [45] Z.Y. Yuan, B.L. Su, *J. Mater. Chem.* 16 (2006) 663–677.
- [46] F.B. Li, X.Z. Li, *Chemosphere* 48 (2002) 1103–1111.